Scientific Reports

https://doi.org/10.1038/s41598-026-57142-9

Article in Press

Paper-based laser-written CoO–graphene biosensor for wireless sweat uric acid detection

Received: 16 March 2026

Accepted: 5 June 2026

Published online: 08 June 2026

Cite this article as: Ganesan V.K., Lee S.P., Low J.H. *et al.* Paper-based laser-written CoO–graphene biosensor for wireless sweat uric acid detection. *Sci Rep* (2026). https://doi.org/10.1038/s41598-026-57142-9

Vinod K. Ganesan, Soon Poh Lee, Jen Hahn Low, Eng Hock Lim, Pei Song Chee & Chun Hui Tan

Paper-Based Laser-Written CoO–Graphene Biosensor for Wireless Sweat Uric Acid Detection

Vinod K Ganesan [a], Soon Poh Lee [a], Jen Hahn Low [a,c], Eng Hock Lim [a,c], Pei Song Chee [a,b,], Chun Hui Tan [a,b,d,*]*

[a] Lee Kong Chian Faculty of Engineering and Science, Universiti Tunku Abdul Rahman, Kajang 43000, Malaysia

[b] Centre of Healthcare Science and Technology, Universiti Tunku Abdul Rahman, Kajang 43000, Malaysia

[c] Centre for Communication Systems and Networks, Universiti Tunku Abdul Rahman, Kajang 43000, Malaysia

[d] Centre for Advanced and Sustainable Materials Research, Universiti Tunku Abdul Rahman, Kajang 43000, Malaysia

* Corresponding author: cheeps@utar.edu.my, tchui@utar.edu.my

Keywords: Sweat-based wearable sensor, Laser-induced graphene (LIG), Non-enzymatic, Flexible paper-based electrodes, NFC-enabled sensing.

ABSTRACT

Uric acid is a critical metabolic biomarker for gout, kidney dysfunction, and cardiovascular disease. Persistent hyperuricemia promotes monosodium urate crystal deposition, triggering recurrent gout flares, chronic joint damage, and systemic inflammation, while early and continuous uric acid monitoring enables timely therapeutic intervention and improved disease outcomes. However, conventional blood tests and enzymatic sensors, although reliable, remain invasive, laboratory-bound, and unsuitable for continuous or point-of-care monitoring. Herein, we report a sustainable one-step strategy to fabricate a nonenzymatic uric acid sensor by direct laser writing on cobalt-treated paper with 455 nm irradiation, producing cobalt oxide–infused graphene. Unlike conventional metal-functionalized laser-induced graphene (LIG), which typically requires multi-step processing and non-biodegradable polymeric substrates, the present approach employs a biomass-derived paper substrate and simultaneously generates conductive graphene and redox-active cobalt oxide nanostructures in a single photothermal process. Furthermore, the incorporated multivalent Co^{2+}/Co^{3+} redox couples act as biomimetic active sites for uric acid oxidation, enabling a flexible low-energy electron-hopping mechanism and enhanced interfacial charge transfer. The resulting porous hybrid electrode provides abundant electroactive sites for efficient sensing performance. Integrated into a flexible near-field communication (NFC) tag, the resulting platform enables wireless, battery-free uric acid monitoring in human sweat. The fabricated

sensor achieved a sensitivity of 9.96 μA·μM^{-1} and a detection limit of 1.08 μM for uric acid sensing. The mechanical robustness is confirmed by minimal resonance frequency variation under bending, shifting only from 13.525 MHz at 0° to 13.575 MHz at 180° (~0.37% relative change). This work establishes a low-cost, scalable, and environmentally sustainable route toward metal oxide-carbon hybrid biosensors, offering a promising pathway for wearable uric acid monitoring and next-generation point-of-care diagnostics.

INTRODUCTION

Uric acid (UA), the end product of purine metabolism, serves as an important biomarker of metabolic health, with abnormal levels linked to gout, hyperuricemia, arthritis, preeclampsia, renal disorders, and cardiovascular complications [1-5]. Among these, gout remains one of the most prevalent conditions, arising from the deposition of UA crystals in joints and surrounding tissues. The disease has become an increasing global health burden, particularly in Southeast Asia, where approximately 4.35 million individuals are affected, reflecting a 21% rise in prevalence between 1990 and 2020 [6]. This trend, driven by lifestyle and dietary changes and an aging population, underscores the need for an accessible diagnostic and continuous monitoring solution [7,8].

Current UA detection methods rely primarily on invasive blood tests and enzymatic assays, which, while reliable, require trained personnel, cause patient discomfort, and are unsuitable for point-of-care or continuous monitoring [9]. Alternative analytical techniques, including fluorometry,

chemiluminescence, colorimetry, high-performance liquid chromatography, and electrochemical methods, have been explored for improved usability and portability [10-12]. Enzyme-based electrochemical sensors, particularly those of uricase, exhibit excellent sensitivity and selectivity by catalyzing UA oxidation to allantoin and hydrogen peroxide, generating proportional electrochemical signals [13-15]. However, the practical implementation of enzymatic systems remains constrained by enzyme instability, cost, and storage requirements, motivating the search for nonenzymatic alternatives [3,16].

Non-enzymatic electrochemical sensors address these challenges by replacing fragile biological components with robust electrocatalytic materials that offer enhanced durability and reproducibility [17-19]. Transition metal oxides, especially cobalt-based nanostructures, have emerged as promising candidates due to their rich redox chemistry, tunable oxidation states, and strong catalytic activity toward UA oxidation. When coupled with conductive carbon-based frameworks such as graphene and carbon nanotubes, these materials exhibit synergistic properties that enhance conductivity, surface area, and active site availability [20-22]. Notable examples include Co_3O_4 nanostructures with diverse morphologies, such as puffy ball–like and nano-berry architectures, demonstrating excellent sensitivity and stability for UA detection in serum [23-26]. Furthermore, cobalt functionalization introduces multivalent Co^{2+}/Co^{3+} redox couples that act as biomimetic sites, accelerating interfacial charge transfer toward uric acid oxidation. Unlike

many other transition metal oxides, which often rely on single oxidation-state transitions, cobalt enables a highly flexible, low-energy electron-hopping mechanism.[27,28]. Despite these advances, most reported methods depend on complex multistep syntheses and rigid electrode platforms, limiting scalability and flexibility.

Laser irradiation has recently emerged as a versatile and sustainable technique for the direct synthesis of laser-induced graphene (LIG) and metal oxide nanostructures, enabling simultaneous fabrication and functionalization of sensing materials in a single step. Among carbon-rich substrates, paper offers unique advantages such as low cost, lightweight, flexibility, and biodegradability. Integrating metal oxides within LIG further enhances electrocatalytic activity and stability through the intimate coupling of active sites [29]. However, most reported approaches rely on CO_2 laser systems, which are energy-intensive and costly, limiting scalability for disposable devices. The 455 nm blue-light diode laser provides a low-energy, sustainable alternative to conventional CO_2 lasers for direct synthesis of LIG and metal oxides. Absorption of 455 nm laser light by the metal precursors induces localized photothermal and photochemical reactions, enabling simultaneous carbonization and metal oxide formation.

While various metal-doped LIGs have been widely demonstrated, their fabrication typically relies on multi-step laser processing, the deposition of metal nanoparticles, or the blending of metal precursors with polyimide[29,30]. However, synthetic polymers like polyimide present environmental concerns

due to their non-biodegradable nature. To address these limitations, biomass alternatives have recently been explored. For instance, Xiao et al. successfully converted cedar wood infused with metal nitride solutions into graphene frameworks embedded via laser scribing [31]. Nevertheless, research regarding the direct, single-step photothermal synthesis of metal oxide/biomass-derived LIG composites for electrochemical sensing detection remains limited.

In this study, we demonstrate a sustainable one-step synthesis of cobalt oxide–infused laser-induced graphene (CoO-LIG) on treated paper using a low-power 455 nm laser, followed by its implementation as a wireless, battery-free UA sensor. This greener alternative to CO_2 laser and hydrothermal methods enables a simpler fabrication approach of CoO-LIG electrodes for non-enzymatic UA detection in sweat. The resulting paper-based CoO-LIG sensor is then seamlessly integrated with near-field communication (NFC) tags for wireless UA monitoring via smartphone. This establishes a low-cost, scalable strategy for fabricating sustainable metal oxide-carbon hybrid, advancing the development of flexible, on-demand biosensors for personalized and point-of-care healthcare.

RESULTS AND DISCUSSION

An overview of the battery-free UA detection system is presented in Figure 1(a), showcasing how the UA level in human sweat is monitored using an optimized CoO-LIG (o-CoO-LIG) NFC tag, and the sensing results are displayed in a user-friendly smartphone application. In this system, a target

warning threshold of 100 µM was established specifically for UA detection in sweat [32,33]. This value serves as an upper baseline limit for gout-precaution, as the typical range for healthy individuals ranges from 20 µM to 80 µM is the typical UA concentration in sweat [34]. When the UA concentration exceeds this threshold, o-CoO-LIG exhibits an increase in resistance, effectively functioning as an electrical switch that disrupts the NFC circuit (Figure1(b)) and triggers a "UA level: Warning". Conversely, when the UA level remains within the safe range, the circuit remains connected, and the smartphone displays "UA level: Safe". This mechanism arises from UA-induced changes in the resonant frequency (f_0) and reflection coefficient (S_{11}) of the o-CoO-LIG NFC tag (Figure 1(c)) across different UA concentrations, thereby altering the wirelessly transmitted signal and enabling concentration-dependent readout on a smartphone application.

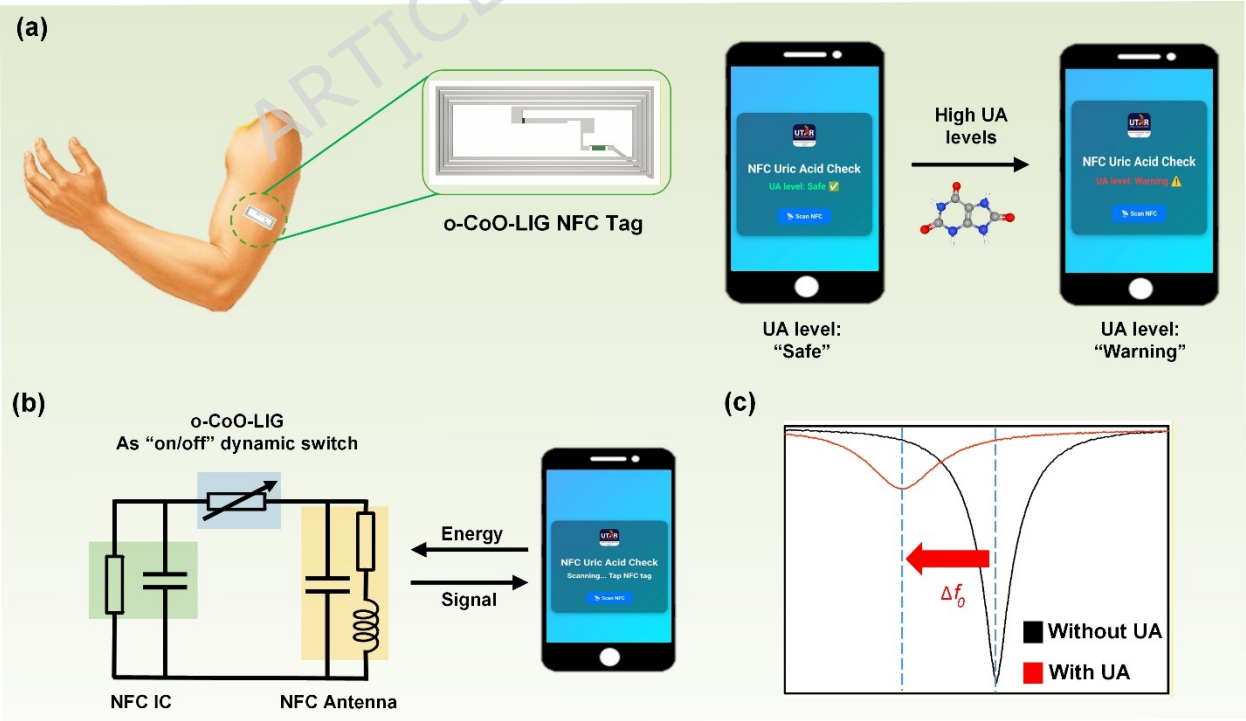

Figure 1. (a) Working principle of battery-free UA detection system using a smartphone to read the o-CoO-LIG NFC tag attached to human skin. (b) Equivalent circuit of the modified NFC tag. (c) Resonance frequency response of the o-CoO-LIG NFC tag in the presence of UA.

The o-CoO-LIG NFC tag was fabricated using a commercial rectangle NFC tag (specifications detailed in Supplementary 1) as the backbone, where a small portion of the conductive trace was selectively removed via laser ablation, as shown in Figure 2(a). The CoO-decorated LIG was optimized to restore the disrupted NFC circuit by achieving a sheet resistance below 257 Ω sq^{-1}, while simultaneously introducing UA sensing functionality by exploiting the high electrochemical activity of CoO toward UA oxidation [35]. Prior to CoO integration, laser parameters were optimized for LIG formation on treated paper to achieve maximum conductivity without compromising structural integrity. Figures 2(b) and 2(c) show that no graphitization occurred at low laser power and high scan speed, while excessive energy at the opposite extreme caused paper ablation. Increasing the laser power and reducing scan speed enhanced graphitization and reduced sheet resistance from 71.88 Ω sq^{-1} to 18.52 Ω sq^{-1}. However, the lowest sheet resistance samples were fragile and prone to cracking, as indicated by the orange boxes in Figure 2(b). Thus, a balanced condition of 0.5 W laser power and 30 mms^{-1} scan speed indicated with a green box in Figure 2(b) was selected, yielding a stable and conductive LIG suitable for CoO decoration. Furthermore, XRD

analysis was performed to assess the formation of graphitic domains in the laser-induced graphene (Supplementary 2).

Since higher CoO content enhances UA redox activity [36], varying concentrations of $Co(NO_3)_2$ precursor were examined. Increasing $Co(NO_3)_2$ concentration from 0.05 M to 1 M led to a sharp rise in sheet resistance from 233.34 Ω sq^{-1} to 87.46 kΩ sq^{-1} (Supplementary Table 1), attributed to the semiconducting nature of Co_3O_4, which impedes conductivity at higher loadings [37]. To balance conductivity and catalytic activity without exceeding the NFC operating frequency range of 13.55 to 13.57 MHz [38], 0.05 M $Co(NO_3)_2$ was selected as the optimal precursor concentration, hereafter referred to as o-CoO-LIG. The S_{11} of the modified NFC tag (Figure 2(d)) confirmed that the o-CoO-LIG restored circuit continuity, exhibiting a f_0 of 13.61 MHz, close to matching the unmodified NFC tag (13.56 MHz), while the open-circuit tag showed no response. Although the modified NFC tag exhibits a f_0 of 13.61 MHz, its impedance bandwidth (defined by $S_{11} \leq -10$ dB) spans from 13.53 to 13.68 MHz overlaps the NFC frequency range. This overlap ensures effective power transfer within the standardized operating range, enabling stable signal detection and reliable smartphone readability [39].

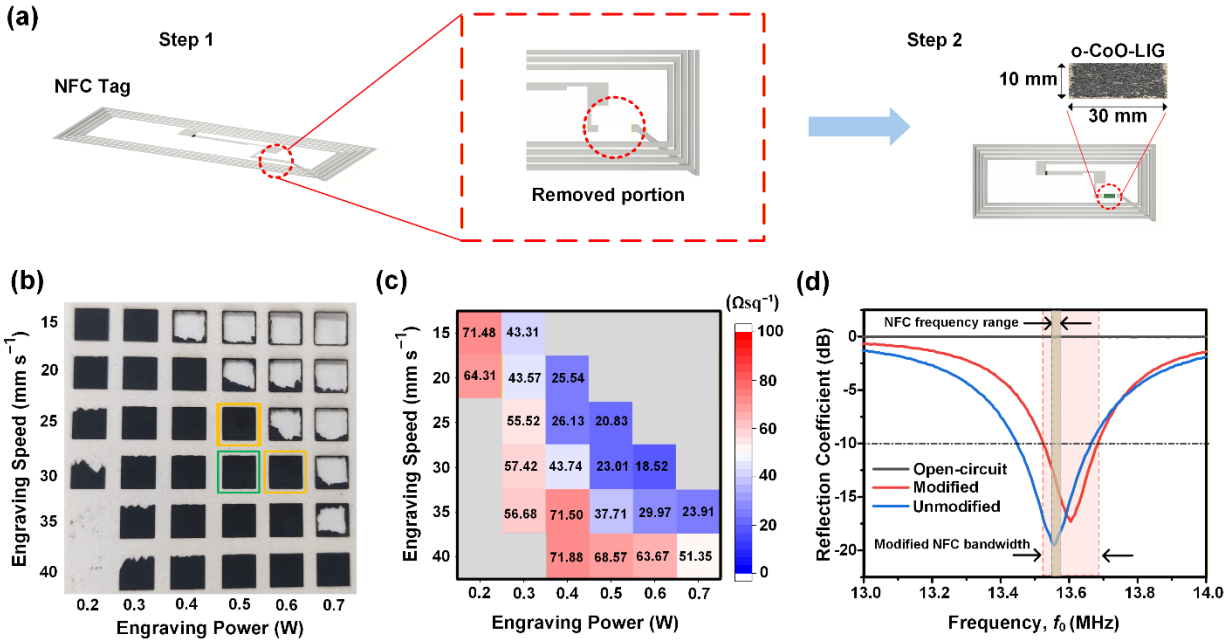

Figure 2. (a) Preparation of the o-CoO-LIG NFC biosensor. (b) Laser parameter optimization matrix and (c) corresponding sheet resistance of the resulting LIG samples. (d) Reflection coefficient (S_{11}) analysis of NFC tag under various conditions. (Horizontal dashed-dot line in (d) indicates the impedance bandwidth)

The electrochemical performance of o-CoO-LIG was evaluated to validate its suitability as a UA sensing element. Cyclic voltammetry (CV) at 50 mVs^{-1} was conducted in 0.1 M phosphate-buffered saline at pH 7 containing 100 µM UA using a three-electrode setup. As shown in Figure 3(a), the LIG sample exhibited purely capacitive behavior, while o-CoO-LIG and commercial CoO-coated nickel tape displayed distinct redox peaks at around 0.12 V and -0.2 V. These peaks confirm the characteristic Co^{2+}/Co^{3+} redox activity consistent with literature reports for cobalt-based biomimetic systems and indicate the crucial role of CoO as the active site for UA sensing [27]. During the laser

engraving process, the intense photothermal energy generated by the laser beam induces the pyrolytic carbonization of the precursor into a porous LIG framework. Concurrently, the extremely high localized temperature triggers rapid nucleation, leading to the in-situ thermal decomposition and localized oxidation of $Co(NO_3)_2$, forming highly active CoO networks directly anchored onto the LIG framework [30]. The integration of CoO within the highly conductive LIG provides a macro-porous architecture that facilitates rapid electron and ion transport, while CoO serves as a robust catalytic active site. SEM-EDX analysis (Figure 3(b) and 3(c)) revealed a porous fibrous morphology with berry-like CoO aggregates anchored on the conductive LIG network, ensuring abundant catalytic sites and efficient electron transport for UA oxidation. Comparison with bare paper (Supplementary Figure 2) further verified successful CoO incorporation.

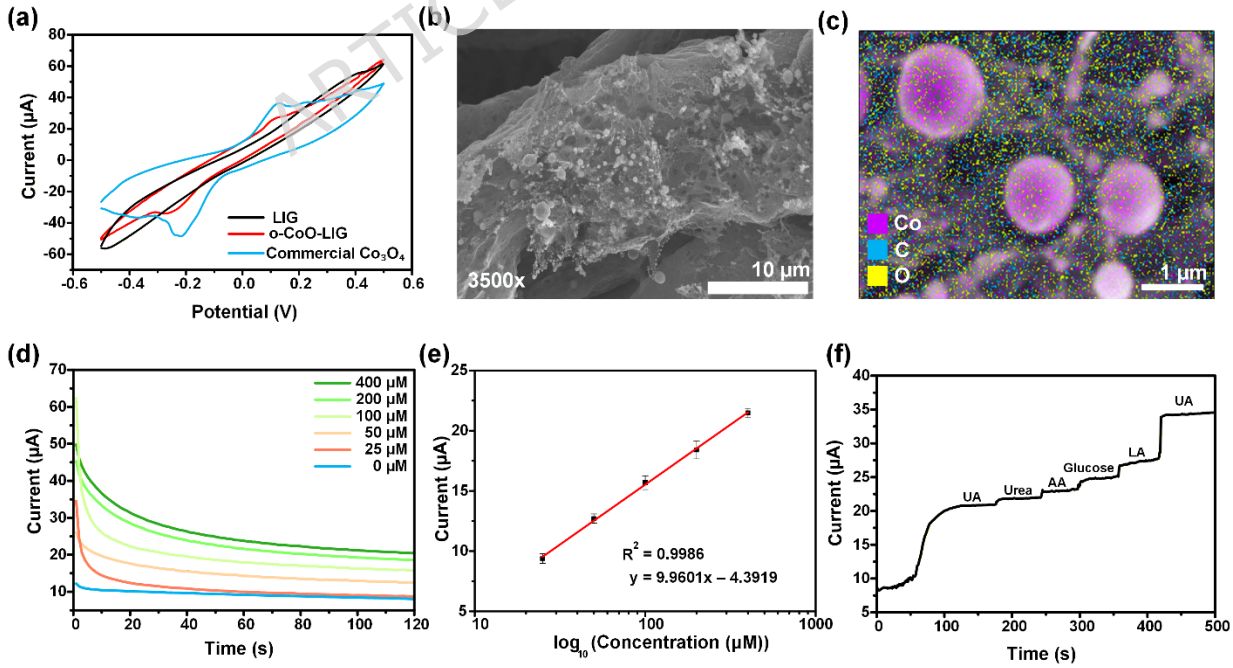

Figure 3. (a) CV response curve of LIG, o-CoO-LIG, and commercial Co_3O_4 in a 0.1 M PBS (pH 7) containing 100 μM UA, (b) SEM image, and (c) EDS mapping of the o-CoO-LIG sample. (d) Chronoamperometric responses to varying UA concentrations and (e) the corresponding calibration curve of the o-CoO-LIG sample. Data are presented as mean values ± standard deviations (n = 3). (f) Interference test of the o-CoO-LIG sample against common organic molecules found in human sweat.

The UA sensing performance of the o-CoO-LIG sensor was further examined using chronoamperometry (CA) at 0.12 V, corresponding to the anodic oxidation potential identified in CV. As shown in Figure 3(d), the steady-state current response increased progressively from 8.46 ± 0.17 μA to 21.48 ± 0.36 μA as the UA concentration rose from 0 μM to 400 μM, exhibiting a logarithmic relationship between current and UA concentration (Figure 3(e)). The limit of detection (LOD) was calculated as follows:

$$\mathrm{LOD} = \frac{3.3\sigma}{S} \qquad (1)$$

Here, the σ represents the standard deviation of the blank response (0 mM UA in PBS), while S denotes the analytical sensitivity obtained from the slope of the semi-logarithmic curve to be 9.96 $\mu A \cdot \mu M^{-1}$. The LOD was calculated to be 1.08 μM (Supplementary 3), confirming the effective UA sensing performance. The linear dependence of current on the natural logarithm of

UA concentration aligns with the logarithmic term in the Nernst equation, indicating that the sensing interface operates in a regime where redox-mediated charge transfer is governed by Nernstian site occupancy [40]. This log-linear behavior, typical of electrochemical sensors with surface-confined mediators, supports an adsorption-controlled sensing mechanism. Furthermore, selectivity tests (Figure 3(f)) verified that common interferents in sweat, including lactic acid (LA), urea, glucose, and ascorbic acid (AA), produced negligible responses compared to UA, demonstrating excellent selectivity [41].

The proposed sensing mechanism of o-CoO-LIG, illustrated in Scheme 1, was further corroborated through FTIR and XRD analyses. As shown in (Figure 4(a) and 4(b)), the o-CoO-LIG exhibited characteristic Co–O lattice vibrations at 594 cm^{-1} and 504 cm^{-1}. After exposure to UA, these bands shifted and narrowed, indicating site-selective coordination of UA that weakens surface Co–O bonds while promoting the oxidation of adjacent domains to CoOOH [42]. In addition, the conductive LIG framework facilitates charge delocalization and rapid electron transport, thereby accelerating this surface redox conversion. Weak vibration features also emerge at 1743 cm^{-1} and 1153 cm^{-1}, corresponding to C=O and C–O vibrations of adsorbed UA oxidation products, respectively, whereas a subtle shoulder at 1634 cm^{-1} was attributed to conjugated C=O vibrations coupled with LIG surface modes [43]. Collectively, these spectral changes confirm that UA oxidation proceeds via Co-mediated surface electron transfer. The introduction of transition metal

oxide dopants effectively modulates the electronic structure of the underlying carbon lattice. This modulation induces interfacial electron redistribution, creating regions of charge density overlap with the target UA molecules. Theoretically, this electron rearrangement enhances adsorption capability and lowers the activation energy barrier for anodic UA oxidation [27,28]. Consequently, the LIG enhances interfacial conductivity and stabilizes transient carbonyl-containing intermediates, thereby establishing an efficient, enzyme-free sensing pathway with high chemical selectivity.

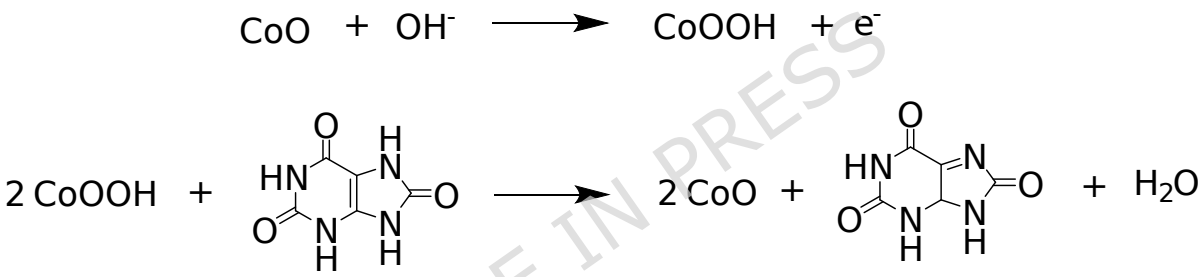

Scheme 1. Sensing mechanism of UA on the o-CoO-LIG sensing layer.

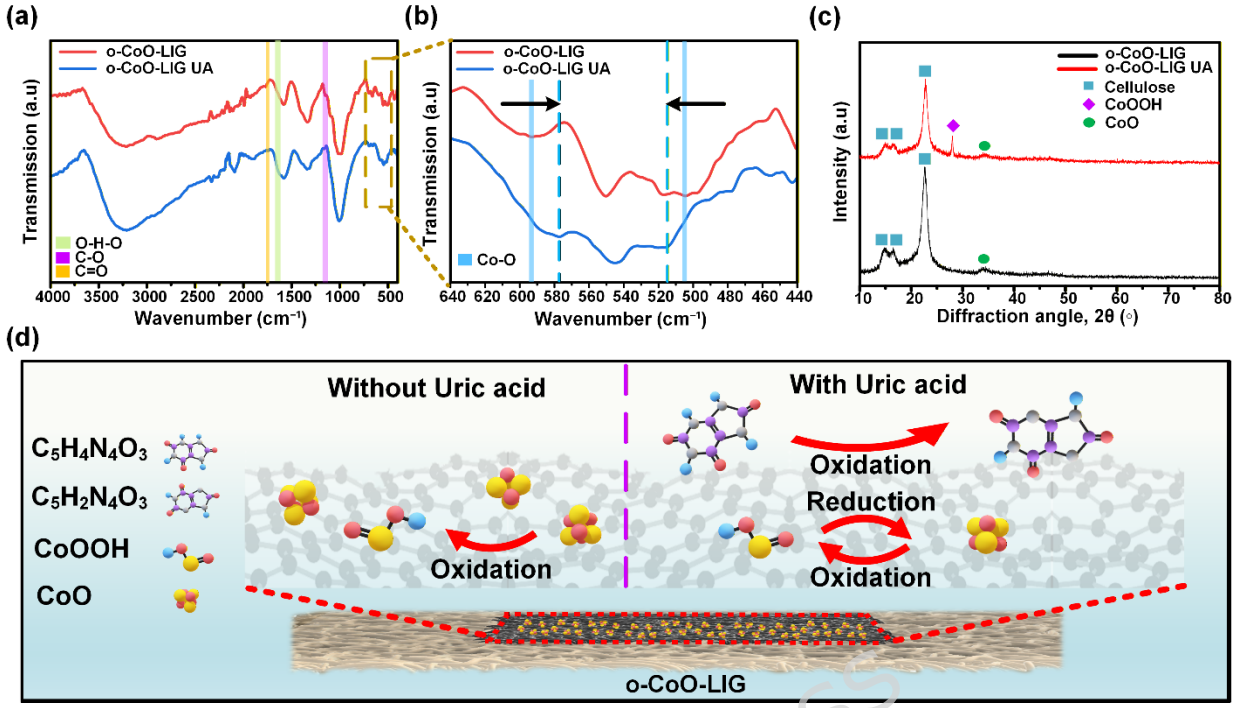

Figure 4. (a) FTIR spectra of o-CoO-LIG sample with and without UA, with (b) magnified view of the fingerprint region. (c) XRD patterns of the o-CoO-LIG sample in the presence and absence of UA. (d) Schematic illustration of UA oxidation mechanism on the o-CoO-LIG sensing layer.

The structural evolution of the Co-based active sites during UA sensing was further examined by XRD analysis (Figure 4(c)). Prior to UA exposure, diffraction peaks appeared at 15.0°, 16.6°, and 22.5°, corresponding to the (110), (110), and (200) planes of cellulose (PDF No. 50-2241), along with a distinct peak at 34.1° indexed to the (111) plane of CoO (PDF No. 42-1300). Upon interaction with UA, an additional peak emerged at 28.0°, assignable to the (120) plane of CoOOH (PDF No. 26-0480), indicating electrochemical oxidation of CoO[44]. This in situ formation of CoOOH generates Co^{3+}–OH

active sites that facilitate electron transfer from UA, promoting its oxidation to dehydrourate, as illustrated in Figure 4(d) [45].

The wireless performance of the o-CoO-LIG NFC tag for UA detection was evaluated across a concentration range of 0 µM to 400 µM by monitoring the shift in the S_{11} spectra (Figure 5(a)) using a vector network analyzer (VNA) connected to a 13.56 MHz test coil positioned directly adjacent to the developed sensor[46]. The corresponding calibration curve can be found in (Supplementary Figure 3). Increased UA concentration raised the loop input impedance (Z_{in}), yielding a shifted f_0 of 13.11 MHz and a maximum magnitude increase of 4.21 dB at 400 µM UA, while concentrations below 100 µM caused a minor shift in f_0. This S_{11} and f_0 can be explained by the increase in tag impedance using the input impedance matching formula (Equation (2)) [47] and the differential coefficient of reflectivity, p (Equation (3)) [48]. Furthermore, this concentration-dependent behavior can be fundamentally elucidated through localized surface electrochemistry and equivalent circuit modeling (Supplementary 4), which systematically maps how interfacial transformations dictate the total input impedance network of the antenna.

$$S_{11} = \frac{Z_{in} - Z_0}{Z_{in} + Z_0}\Big|_{Z_0=50\Omega} \tag{2}$$

$$p = \sqrt{\frac{(R_L + R_r)^2 + X_L^2}{(R_L + R_r)^2 + X_L^2}} \tag{3}$$

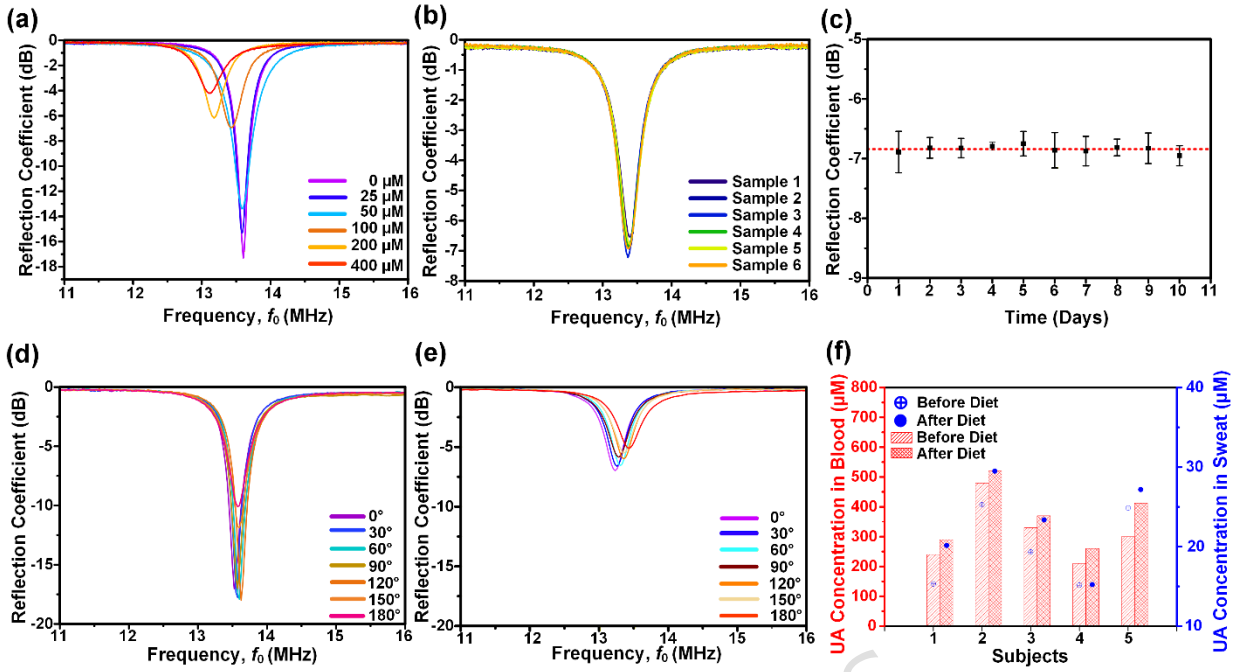

Figure 5. (a) S_{11} response of o-CoO-LIG NFC tag under varying UA concentrations. (b) Reproducibility and (c) long-term stability of the tag evaluated in 100 μM UA. (d) Measured S_{11} response of o-CoO-LIG NFC tag under various bending angles without and (e) with 100 μM UA. (f) Monitoring of the sweat UA levels using the o-CoO-LIG NFC tag, with parallel comparison to fingertip blood UA measurements. Data are presented as mean values ± standard deviations (n = 5).

When UA exceeds 100 μM, the high impedance disconnects the NFC circuit, rendering the tag unreadable at 13.43 MHz, as its impedance bandwidth falls outside the NFC frequency range. To evaluate the reliability of the o-CoO-LIG NFC tag, descriptive statistical analysis was applied to the experimental datasets. Reproducibility was evaluated across six independent sensor tags (n = 6) under identical testing conditions (Figure 5(b)), yielding a mean S_{11} value of −6.84 dB with a standard deviation of 0.24 dB and a relative standard

deviation (RSD) of 3.53%, thereby confirming consistent sensor performance. Long-term stability was assessed over a 10-day period using a total of thirty fabricated tags, where three randomly selected tags were measured each day (n = 3 daily repetitions) to calculate the daily mean values (Figure 5(c)). The resulting stability data exhibited minimal day-to-day variation in the S_{11} response, with an RSD of 0.81%, confirming highly repeatable sensing performance.

The mechanical flexibility of the o-CoO-LIG NFC tag was examined by mounting the antenna onto the 3D printed PLA ring with incremental bending angles of 30° and recording the corresponding S_{11}. As shown in Figure 5d, the S_{11} responses exhibit negligible variation of approximately 0.37% across different bending states, where the frequency changes from 13.53 MHz at 0° to 13.58 MHz at 180°, reflecting the excellent robustness of the o-CoO-LIG NFC tag. The substantial overlap among the resonance profiles ensures effective impedance matching and power transfer within the designated operating band, enabling reliable signal acquisition and consistent smartphone readability. The test was repeated by adding 100 µM of UA (Figure 5(e)) to the o-CoO-LIG NFC tag and showed minimal changes in response (Supplementary Table 2), with the S_{11} magnitude varying approximately 23% and the f_0 shifting from 13.25 MHz at 0° to 13.43 MHz at 180°. The responses at all bending angles remain undetectable by the smartphone, further confirming its stable sensing on high UA concentration.

The developed sensor tag was evaluated on a phantom (artificial) skin model. An artificial sweat containing 100 μM UA was introduced to assess the practical functionality of the sensor tag, as shown in Supplementary Video 1. The o-CoO-LIG NFC tag becomes unreadable when scanned with a smartphone, and the mobile application displays “UA level: Warning” after 10 seconds of unreadability.

The o-CoO-LIG NFC tag was further validated for UA detection in authentic human sweat and benchmarked against blood UA levels. Sweat samples were collected using a filter paper strip after aerobic exercise to minimize interference from anaerobic exercise–induced UA production. The human subject was first monitored for UA level condition under fasting conditions and tested again after consuming a purine-rich meal. The UA level results were compared with fingertip blood measurements from five subjects (n = 5) using a commercial UA analyzer concurrently with the o-CoO-LIG NFC tag, as shown in (Supplementary Figure 6). For all subjects, an increase in UA concentration after meals was consistently observed in both blood-based measurements and sweat-based detection. Notably, the shift in S_{11} is consistent with the corresponding increase in blood UA levels, suggesting a positive correlation between the o-CoO-LIG NFC tag response and the blood test results (Supplementary 5). This trend is further supported by the observed rise in UA concentration in sweat after purine intake, which arises from purine metabolism wherein adenine and guanine are oxidized to UA via

hypoxanthine and xanthine intermediates [49], as summarized in Equations (4)-(6).

$$\text{Hypoxanthine} \xrightarrow[\text{xanthine oxidase}]{} \text{Xanthine} \xrightarrow[\text{xanthine oxidase}]{} \text{Uric Acid} \quad (4)$$

$$\text{Hypoxanthine} + O_2 + H_2O \xrightarrow[\text{xanthine oxidase}]{} \text{Xanthine} + H_2O_2 \quad (5)$$

$$\text{Xanthine} + O_2 + H_2O \xrightarrow[\text{xanthine oxidase}]{} \text{Uric Acid} + H_2O_2 \quad (6)$$

CONCLUSION

Herein, the o-CoO-LIG NFC tag achieved UA sensing performance comparable to previously reported sensors, with similar LOD (Supplementary Table 3). Importantly, the laser-irradiation fabrication route offers a more sustainable alternative to conventional CO_2 laser and hydrothermal methods, enabling direct, mask-free patterning on flexible substrates in a single step. This facile, scalable approach reduces preparation complexity while providing precise control over electrode architecture. Additionally, the o-CoO-LIG NFC tag allows wireless, battery-free UA detection, where such demonstrations are limited in prior studies. These combined features of simple fabrication and wireless functionality highlight the potential of this platform for practical and portable biochemical sensing applications.

METHODS

Fabrication of CoO decorated LIG (CoO-LIG) electrode

The CoO-LIG electrode was fabricated using a modified filter paper substrate through a sequential chemical treatment and laser-engraving processes as summarized below:

Preparation of carbon-rich $Co(NO_3)_2$ fire-retardant solution

Initially, an aqueous fire-retardant solution was prepared by dissolving 5 g of boric acid (≥99.5%, Sigma-Aldrich) and 5 g of borax (≥99.9%, Sigma-Aldrich) in 200 mL of deionized water. 0.8 g of lignosulfonate (Sigma-Aldrich) and 0.1 g of 2-hydroxyethyl cellulose (average Mv-1,300,000, Sigma-Aldrich) were subsequently incorporated into the solution as a carbonaceous precursor for LIG formation. Cobalt nitrate hexahydrate ($Co(NO_3)_2 \cdot 6H_2O$, ≥98%, Sigma-Aldrich) was then added to the mixture to serve as the cobalt source for cobalt oxide formation. The resulting solution was magnetically stirred at room temperature for 30 minutes.

Synthesis of CoO-LIG

The filter paper substrates were immersed in the carbon-rich $Co(NO_3)_2$ fire-retardant solution for 10 min to ensure thorough impregnation, then dried on a hot plate at 100 °C. The treated filter papers were then subjected to laser engraving using a blue diode laser 455 nm, xTools M1 under optimized parameters (0.5 W laser power and 30 mms^{-1} scan speed), resulting in the in situ formation of LIG decorated with cobalt oxide nanoparticles.

Fabrication of o-CoO-LIG NFC tag

The o-CoO-LIG NFC tag was fabricated by introducing a deliberate cut in the conductive trace of a commercial 13.56 MHz NFC tag to form an open circuit.

A prepared o-CoO-LIG sample was aligned nicely across the cut region to act as the functional bridge for reconnection of the NFC circuit. Scoth tape was applied to secure the o-CoO-LIG sample on top of the NFC tag, resulting in a reliable electrical connection. Hence, restoring the resonance of the tag and enabling wireless operation.

Material and tag characterization

A four-point probe system (Ossila T2001A3) was employed to acquire the sheet resistance of the as-synthesized o-CoO-LIG sample. The wireless sensing characteristics were investigated via S_{11} parameter measurements using a vector network analyzer (VNA, Keysight E5061B). Electrochemical performance was evaluated through cyclic voltammetry (CV), and chronoamperometry (CA) using ZIVE SP1 in a three-electrode configuration, comparing commercial cobalt oxide, the o-CoO-LIG, and pristine LIG. The surface morphology and elemental distribution of the fabricated LIG–cobalt oxide were examined using scanning electron microscopy (SEM, Hitachi S3400N) coupled with energy-dispersive X-ray spectroscopy (EDX, Ametek Apollo X). The functional groups present on the electrode surface were analyzed using Fourier-transform infrared spectroscopy (FTIR, PerkinElmer Spectrum Two) to elucidate the sensing mechanism, in conjunction with X-ray diffractometry (XRD, Shimadzu XRD-6000) under Cu Kα radiation for phase identification and crystal structure analysis. The mechanical flexibility was examined by conforming the fabricated o-CoO-LIG NFC tag onto a 3D-printed arch with the bending angle adjusted in incremental steps of 30°, and the corresponding frequency response was recorded using VNA.

Non-invasive uric acid detection method

This study involved exclusively healthy human participants with no prior diagnosis of gout. Written informed consent was obtained from all participants prior to enrolment. All procedures involving human participants were performed in accordance with relevant guidelines and regulations. The study protocol was reviewed and approved by the Universiti Tunku Abdul Rahman's Scientific and Ethical Review Committee (SERC) (Approval No. U/SERC/56(B)-81/2025). UA detection in sweat was evaluated under controlled dietary conditions. The subject underwent overnight fasting for 10 hours, after which baseline UA levels were measured in blood and sweat. The UA concentration in blood was obtained at a licensed pharmacy using a commercial UA detection device and recorded as a reference. The UA in sweat was obtained through aerobic exercise. The sweat was collected through a filter paper strip, which was subsequently placed onto the fabricated o-CoO-LIG NFC tag. The corresponding resonance frequency was then measured using a VNA. Following the baseline measurements, the subject consumed a purine-rich meal, and similar measurements were conducted after 2 hours.

AUTHOR INFORMATION

Corresponding Authors

Chun Hui Tan - *Lee Kong Chian Faculty of Engineering and Science, Universiti Tunku Abdul Rahman, Kajang 43000, Malaysia; Centre of*

Healthcare Science and Technology, Universiti Tunku Abdul Rahman, Kajang 43000, Malaysia; Centre for Advanced and Sustainable Materials Research, Universiti Tunku Abdul Rahman, Kajang 43000, Malaysia; https://orcid.org/0000-0002-9726-0866; Email: tchui@utar.edu.my

Pei Song Chee - *Lee Kong Chian Faculty of Engineering and Science, Universiti Tunku Abdul Rahman, Kajang 43000, Malaysia; Centre of Healthcare Science and Technology, Universiti Tunku Abdul Rahman, Kajang 43000, Malaysia;* https://orcid.org/0000-0001-7165-7788; Email: cheeps@utar.edu.my

Authors

Vinod K Ganesan - *Lee Kong Chian Faculty of Engineering and Science, Universiti Tunku Abdul Rahman, Kajang 43000, Malaysia;* https://orcid.org/0009-0001-2097-8642

Soon Poh Lee - *Lee Kong Chian Faculty of Engineering and Science, Universiti Tunku Abdul Rahman, Kajang 43000, Malaysia;* https://orcid.org/0000-0001-8072-8322

Eng Hock Lim - *Lee Kong Chian Faculty of Engineering and Science, Universiti Tunku Abdul Rahman, Kajang 43000, Malaysia; Centre for Communication Systems and Networks, Universiti Tunku Abdul Rahman, Kajang 43000, Malaysia;* https://orcid.org/0000-0001-5301-1115

Jen Hahn Low - *Lee Kong Chian Faculty of Engineering and Science, Universiti Tunku Abdul Rahman, Kajang 43000, Malaysia; Centre for Communication Systems and Networks, Universiti Tunku Abdul Rahman, Kajang 43000, Malaysia;* https://orcid.org/0000-0001-5321-6516

Author Contributions

Vinod K Ganesan Writing – original draft, Investigation, Formal analysis, Data curation, Conceptualization; **Soon Poh Lee** Writing – review & editing, Validation, Investigation, Formal analysis, Data curation; **Eng Hock Lim** Writing – review & editing, Visualization, Validation, Supervision, Resources; **Jen Hahn Low** Visualization, Validation, Methodology, Investigation, Formal analysis; **Pei Song Chee** Writing – review & editing, Visualization, Validation, Supervision, Resources; **Chun Hui Tan** Writing – review & editing, Validation, Supervision, Resources, Project administration, Investigation, Funding acquisition, Conceptualization.

Notes

The authors declare no competing financial interest.

FUNDING DETAILS

This research was supported by the Ministry of Higher Education Malaysia (MoHE), through the Fundamental Research Grant Scheme (FRGS/1/2024/STG05/UTAR/02/2) and Universiti Tunku Abdul Rahman (UTAR) Research Fund (IPSR/RMC/UTARRF/2023-C2/T02).

ABBREVIATIONS

LIG, laser-induced graphene; CoO-LIG, cobalt oxide-infused laser-induced graphene; NFC, near-field communication; UA, uric acid; o-CoO-LIG, optimized CoO-LIG; CV, cyclic voltammetry; CA, chronoamperometry; LOD, limit of detection

DATA AVAILABILITY

The authors declare that the data supporting the findings of this study are available within the article and its Supplementary Information. Additional raw data files, in alternative formats if required, are available from the corresponding author upon reasonable request.

REFERENCES

1 Saito, Y., Tanaka, A., Node, K. & Kobayashi, Y. Uric acid and cardiovascular disease: a clinical review. *Journal of cardiology* **78**, 51-57 (2021).
2 Sun, H.-l. *et al.* Function of uric acid transporters and their inhibitors in hyperuricaemia. *Frontiers in pharmacology* **12**, 667753 (2021).
3 Schlesinger, N., Pérez-Ruiz, F. & Lioté, F. Mechanisms and rationale for uricase use in patients with gout. *Nature Reviews Rheumatology* **19**, 640-649 (2023).
4 Kuwabara, M. *et al.* Update in uric acid, hypertension, and cardiovascular diseases. *Hypertension Research* **46**, 1714-1726 (2023).
5 Wen, S., Arakawa, H. & Tamai, I. Uric acid in health and disease: From physiological functions to pathogenic mechanisms. *Pharmacology & Therapeutics* **256**, 108615 (2024).
6 Bernama. *Gout: A Growing Health Concern ni Malaysia*, <https://www.bernama.com/en/news.php?id=2424849> (2025).
7 Yang, Y. & Liu, Z. The changing burden of gout in adults aged 70 and above based on the global burden of disease 2019. *Frontiers in Public Health* **13**, 1455726 (2025).
8 Smith, E. *et al.* The global burden of gout: estimates from the Global Burden of Disease 2010 study. *Annals of the rheumatic diseases* **73**, 1470-1476 (2014).
9 Hu, Y. *et al.* Prolonged monitoring and risk management of hyperuricemia using interference-resistant wearable bioelectronics. *Device* (2025).

10 Tripathi, R. M. & Chung, S. J. Ultrasensitive and selective colorimetric detection of uric acid using peroxidase mimetic activity of biogenic palladium nanoparticles. *Luminescence* **38**, 1330-1338 (2023).
11 Moriiwa, Y. *et al.* Colorimetric and fluorometric determination of uric acid by a suspension-based assay using enzyme-immobilized micro-sized particles. *Analytical Sciences* **40**, 951-958 (2024).
12 Kang, L. *et al.* Improved ultra-high performance liquid chromatographic method for simultaneous determination of five gout-related metabolites in human serum. *Journal of Separation Science* **44**, 954-962 (2021).
13 Liu, Y. *et al.* Uric acid and creatinine biosensors with enhanced room-temperature storage stability by a multilayer enzyme matrix. *Analytica Chimica Acta* **1227**, 340264 (2022).
14 Guan, H., Peng, B., Gong, D., Han, B. & Zhang, N. Electrochemical Enhanced Detection of Uric Acid Based on Peroxidase-like Activity of Fe3O4@ Au. *Electroanalysis* **33**, 1736-1745 (2021).
15 Stephanie, R., Lee, D. Y., Park, C. Y. & Park, T. J. Transition metal complex-incorporated polyaniline as a platform for an enzymatic uric acid electrochemical sensor. *Analyst* **148**, 1442-1450 (2023).
16 Tvorynska, S., Barek, J. & Josypčuk, B. Flow amperometric uric acid biosensors based on different enzymatic mini-reactors: A comparative study of uricase immobilization. *Sensors and Actuators B: Chemical* **344**, 130252 (2021).
17 Khan, M. *et al.* Vertically oriented zinc oxide nanorod-based electrolyte-gated field-effect transistor for high-performance glucose sensing. *Analytical Chemistry* **94**, 8867-8873 (2022).
18 Masrat, S. *et al.* Electrochemical sensing of uric acid with zinc oxide nanorods decorated with copper oxide nanoseeds. *ACS Applied Nano Materials* **6**, 16615-16624 (2023).
19 Xu, Z. *et al.* A conducting polymer PEDOT: PSS hydrogel based wearable sensor for accurate uric acid detection in human sweat. *Sensors and Actuators B: Chemical* **348**, 130674 (2021).
20 Wang, Y.-X. *et al.* Boron-doped graphene quantum dots anchored to carbon nanotubes as noble metal-free electrocatalysts of uric acid for a wearable sweat sensor. *ACS Applied Nano Materials* **5**, 11100-11110 (2022).
21 Fu, L. *et al.* An electrochemical sensor based on reduced graphene oxide and ZnO nanorods-modified glassy carbon electrode for uric acid detection. *Arabian Journal for Science and Engineering* **41**, 135-141 (2016).
22 Aparna, T., Sivasubramanian, R. & Dar, M. A. One-pot synthesis of Au-Cu2O/rGO nanocomposite based electrochemical sensor for selective and simultaneous detection of dopamine and uric acid. *Journal of Alloys and Compounds* **741**, 1130-1141 (2018).

23 Quan, C., Chen, W., Yang, M. & Hou, Y. Electrochemical sensor using cobalt oxide-modified porous carbon for uric acid determination. *Microchimica Acta* **190**, 401 (2023).
24 Masrat, S. *et al.* Electrochemical ultrasensitive sensing of uric acid on non-enzymatic porous cobalt oxide nanosheets-based sensor. *Biosensors* **12**, 1140 (2022).
25 Demirkan, B. *et al.* Composites of bimetallic platinum-cobalt alloy nanoparticles and reduced graphene oxide for electrochemical determination of ascorbic acid, dopamine, and uric acid. *Scientific reports* **9**, 12258 (2019).
26 Khan, M. I. *et al.* Non-enzymatic electrochemical dopamine sensing probe based on hexagonal shape zinc-doped cobalt oxide (Zn-Co2O4) nanostructure. *Microchimica Acta* **189**, 37 (2022).
27 Hu, F. X. *et al.* Single-atom cobalt-based electrochemical biomimetic uric acid sensor with wide linear range and ultralow detection limit. *Nano-micro letters* **13**, 7 (2021).
28 Sindhu, P., Ananthram, K., Jain, A., Tarafder, K. & Ballav, N. Charge-transfer interface of insulating metal-organic frameworks with metallic conduction. *Nature Communications* **13**, 7665 (2022).
29 Ye, R. *et al.* In situ formation of metal oxide nanocrystals embedded in laser-induced graphene. *ACS nano* **9**, 9244-9251 (2015).
30 Ren, M., Zhang, J. & Tour, J. M. Laser-induced graphene synthesis of Co3O4 in graphene for oxygen electrocatalysis and metal-air batteries. *Carbon* **139**, 880-887 (2018).
31 Han, X. Tour, Laser-Induced Graphene from Wood Impregnated with Metal Salts and Use in Electrocatalysis. ACS Appl. *Nano Mater* **1**, 5053 (2018).
32 Yang, Y. *et al.* A laser-engraved wearable sensor for sensitive detection of uric acid and tyrosine in sweat. *Nature biotechnology* **38**, 217-224 (2020).
33 Min, J. *et al.* Skin-interfaced wearable sweat sensors for precision medicine. *Chemical reviews* **123**, 5049-5138 (2023).
34 Gao, W. *et al.* An integrated wearable photo-electrochemical sensor for visible light amplified uric acid monitoring in sweat. *Biosensors and Bioelectronics*, 117892 (2025).
35 Hussain, M. M., Rahman, M. M., Asiri, A. M. & Awual, M. R. Non-enzymatic simultaneous detection of L-glutamic acid and uric acid using mesoporous Co 3 O 4 nanosheets. *RSC advances* **6**, 80511-80521 (2016).
36 Nagal, V. *et al.* Hexagonal cobalt oxide nanosheet-based enzymeless electrochemical uric acid sensor with improved sensitivity. *New Journal of Chemistry* **47**, 4206-4212 (2023).
37 Nagal, V. *et al.* A non-enzymatic electrochemical sensor composed of nano-berry shaped cobalt oxide nanostructures on a glassy carbon electrode for uric acid detection. *New Journal of Chemistry* **46**, 12333-12341 (2022).

38 Regulations, I. R. & II-Frequencies, C. ARTICLE 5 Frequency allocations. *Section IV–Table of Frequency Allocations* **956** (2012).
39 Low, J.-H., Chee, P.-S. & Lim, E.-H. Liquid EBG-backed stretchable slot antenna for human body. *IEEE Transactions on Antennas and Propagation* **70**, 9120-9129 (2022).
40 Li, J., Kumar, A., Johnson, B. A. & Ott, S. Experimental manifestation of redox-conductivity in metal-organic frameworks and its implication for semiconductor/insulator switching. *Nature Communications* **14**, 4388 (2023).
41 Chen, F. *et al.* A wearable electrochemical biosensor utilizing functionalized Ti3C2T x MXene for the real-time monitoring of uric acid metabolite. *Analytical Chemistry* **96**, 3914-3924 (2024).
42 Huang, Z. *et al.* Study on the oxidation process of cobalt hydroxide to cobalt oxides at low temperatures. *RSC Advances* **6**, 80059-80064 (2016).
43 Atta, D., Refaat, A., Ashery, A. & Ibrahim, M. Graphene oxide: Synthesis and laser spectroscopy approach. *Optical Materials: X* **22**, 100302 (2024).
44 Sun, X. *et al.* Metallic CoO/Co heterostructures stabilized in an ultrathin amorphous carbon shell for high-performance electrochemical supercapacitive behaviour. *Journal of Materials Chemistry A* **7**, 372-380 (2019).
45 Zahed, M. A. *et al.* Ex situ hybridized hexagonal cobalt oxide nanosheets and RGO@ MWCNT based nanocomposite for ultra-selective electrochemical detection of ascorbic acid, dopamine, and uric acid. *Journal of The Electrochemical Society* **166**, B304-B311 (2019).
46 Charkhabi, S. *et al.* Monitoring wound health through bandages with passive LC resonant sensors. *ACS sensors* **6**, 111-122 (2020).
47 Dong, L., Wang, L.-F. & Huang, Q.-A. Implementation of multiparameter monitoring by an LC-type passive wireless sensor through specific winding stacked inductors. *IEEE Internet of Things Journal* **2**, 168-174 (2014).
48 Terman, F. E. *Radio engineers' handbook*. (1943).
49 Maiuolo, J., Oppedisano, F., Gratteri, S., Muscoli, C. & Mollace, V. Regulation of uric acid metabolism and excretion. *International journal of cardiology* **213**, 8-14 (2016).